Applied Catalysis B: Environmental 250 (2019) 150–162

Contents lists available at ScienceDirect

Applied Catalysis B: Environmental

journal homepage: www.elsevier.com/locate/apcatb

Construction of g-C_3N_4/PDI@MOF heterojunctions for the highly efficient visible light-driven degradation of pharmaceutical and phenolic micropollutants

Yuanyuan Li[a], Yu Fang[a], Zhenlei Cao[a], Najun Li[a,b], Dongyun Chen[a,b], Qingfeng Xu[a,b,*], Jianmei Lu[a,b,*]

[a] College of Chemistry, Chemical Engineering and Materials Science, Collaborative Innovation Center of Suzhou Nano Science and Technology, Soochow University, Suzhou, Jiangsu 215123, China

[b] National Center for International Research on Intelligent Nano-Materials and Detection Technologies in Environment Protection, Suzhou, Jiangsu 215123, China

ARTICLE INFO

Keywords:
g-C_3N_4/PDI
MOF
Visible light
Photocatalysis
Fenton-like reaction

ABSTRACT

A novel g-C_3N_4/PDI@MOF heterojunction was synthesized by the *in situ* growth of NH_2-MIL-53(Fe) onto the g-C_3N_4/PDI layer. The heterojunction was applied as a photocatalyst for the removal of pharmaceutical and phenolic micropollutants in the present of H_2O_2 and visible LED light ($420 < \lambda < 800$ nm). The synergistic heterojunction displays excellent photocatalytic performance for the removal of several water-soluble and toxic organic pollutants (50 ppm) under visible light irradiation, with a maximum efficiency of up to 90% (1 h) for tetracycline (TC), 78% (2.5 h) for carbamazepine (CBZ), 100% (10 min) for bisphenol A (BPA) and 100% (30 min) for p-nitrophenol (PNP). Furthermore, the low concentration of phenolic organic pollutants (2 ppm) can also be rapidly degraded into small molecules (analyzed by HPLC) within 10 min. This performance is superior to some previously reported visible-light photocatalysts. The improved photocatalytic activity is attributed to the efficient formation of heterojunctions derived from the interface contact and electronic band structure matching between g-C_3N_4/PDI and NH_2-MIL-53(Fe), which is beneficial to charge separation and facilitates the photodegradation process. Repeated experimental studies and structural analysis of photocatalyst before and after degradation (XRD and FT-IR) demonstrated that the photocatalyst exhibits good stability and reusability. This work provides a new insight into the construction of heterojunction photocatalysts based on Fe-MOF for the heterogeneous photodegradation of organic contaminants with H_2O_2 under visible light.

1. Introduction

Water contamination caused by organic pollutants has attracted worldwide attention due to its long-term harm to human beings and aquatic organisms [1]. The disposal of toxic contaminants, such as pharmaceutical and phenolic compounds, is difficult with conventional chemical treatment [2], and these contaminants can be commonly found on surfaces water in/around China and other areas [3]. The use of heterogeneous photocatalysts that utilize renewable solar energy may allow for an effective method for the degradation of pollutants [4] such as TiO_2 [5], ZnO [6], CeO_2 [7], CdS [8], etc. Nevertheless, the practical application of TiO_2 is greatly limited by its poor solar energy conversion efficiency due to its wide band gap of approximately 3.2 eV. Thus, there is still an urgent need to discover materials with efficient photocatalytic behavior in the visible light region. The ideal material should exhibit: (1) broad visible-light absorption; (2) excellent separation of photogenerated charge carriers; (3) high stability and reusability.

Two-dimensional (2D) graphitic carbon nitride (g-C_3N_4), a promising organic polymer photocatalyst with a narrow band gap of approximately 2.7 eV, has been utilized in water splitting and for the decomposition of organic pollutants under visible light irradiation [9–11]. It can be easily synthesized via the simple thermal condensation of nitrogen-bearing precursors, and its inexpensive and sustainable nature, and high thermal and chemical stability, make g-C_3N_4 suitable for solar-energy conversion [12,13]. In addition, many organic syntheses have been developed to rationally tune the chemical structure and improve the photocatalytic performance because of its versatile

* Corresponding author at: College of Chemistry, Chemical Engineering and Materials Science, Collaborative Innovation Center of Suzhou Nano Science and Technology, Soochow University, Suzhou, Jiangsu 215123, China.
E-mail addresses: xuqingfeng@suda.edu.cn (Q. Xu), lujm@suda.edu.cn (J. Lu).

https://doi.org/10.1016/j.apcatb.2019.03.024
Received 13 November 2018; Received in revised form 1 February 2019; Accepted 9 March 2019
Available online 09 March 2019
0926-3373/ © 2019 Published by Elsevier B.V.

structure [14,15]. For instance, g-C_3N_4 doped with pyromellitic diimide (PDI), namely g-C_3N_4/PDI, can efficiently tailor its band structure toward specific photoreactions [16,17]. Once electron deficient aromatic diimides are introduced into the framework of g-C_3N_4, the energy of the conduction band can be significantly reduced. As is well known, electronic band structure matching in the heterojunction photocatalyst is beneficial to the separation of photogenerated charge carriers for improving photocatalytic activity [18,19]. Thus, the synthesis of heterojunction composites by combining these bandgap-modified g-C_3N_4 with other semiconductor, could efficiently suppress the recombination of photo-induced electronic-holes, which may result in greater photocatalytic efficiency.

Photoactive metal–organic frameworks (MOF) have received widespread attention for the photocatalytic decomposition of organic pollutants owing to their adjustable structural composition and high surface area and porosity [20]. They also allow for the good accommodation and rapid mass transport of guest molecules [21]. Until now, most research has focused on the fabrication of g-C_3N_4 and MOF composites for enhancing the separation of photo-induced electron-holes [22–26]. However, the impact of MOF/g-C_3N_4 composites on photocatalytic activity, via the adjustment of the chemical structure of g-C_3N_4 by organic reactions, has not been widely reported. The effect of the electronic band structure of the semiconductors on the carrier transport of the heterojunction materials remains unclear. Furthermore, Fe-contained MOFs have been extensively studied due to iron is an abundant element in earth and the iron–oxo clusters present in Fe-based MOFs exhibit a wide absorption range in the visible region [27,28]. For instance, MIL-53(Fe) shows efficient photocatalytic performance for simultaneously the reduction of Cr (VI) and removal of organic pollutants under the visible light [29,30]. Based on the above studies, we hypothesize that Fe-based MOFs and polymer photocatalyst (g-C_3N_4/PDI) can be successfully hybridized to form a heterojunction, the heterojunction interface can serve as a robust platform for the transportation of photo-induced electrons from the conductive band of g-C_3N_4/PDI to that of the Fe-based MOFs. Ultimately, the photocatalytic activity of composites can be dramatically improved for the photodegradation of organic pollutants.

In the present work, we designed and synthesized a g-C_3N_4/PDI@MOF (CPM) photocatalyst, as illustrated in Scheme 1. Firstly, the g-C_3N_4/PDI was obtained by a calcination process of pyromellitic dianhydride and melem [17]. The NH_2-MIL-53(Fe) grows then on the surface of g-C_3N_4/PDI by a solvothermal process. The resulting CPM composites were fully characterized by XRD, FT-IR, TG, SEM, XPS and UV–vis spectroscopy. The band position of the prepared g-C_3N_4/PDI matches well with that of the synthesized NH_2-MIL-53(Fe). The photocatalytic performance of the photocatalyst was evaluated with respect to the removal of pharmaceutical and phenolic micropollutants with the assistance of visible LED light. Its high performance can mostly be attributed to the synergistic heterojunction between Fe-MOF and g-C_3N_4/PDI, which facilitates the transfer of photo-induced electrons. The stability and recyclability of the CPM composite was investigated in detail. Based on photoluminescence (PL), photocurrent and electron spin resonance (ESR) analysis, a possible photocatalytic mechanism has been proposed.

2. Experimental

2.1. Materials

Melamine, ferric chloride hexahydrate ($FeCl_3{\cdot}6H_2O$), pyromellitic dianhydride (PMDA), 2-aminoterephthalic acid (NH_2-BDC), 5,5-dimethyl-l-pyrroline-*N*-oxide (DMPO), tetracycline (TC) hydrochloride, carbamazepine (CBZ), bisphenol A (BPA), p-nitrophenol (PNP), and p-benzoquinone (BQ) were obtained from TCI (Shanghai) Development Co. Ltd. Methanol (MeOH), *N,N*-dimethyl formamide (DMF), H_2O_2 (30%, w/w) and tert-butyl alcohol (TBA) were purchased from Sinopharm Chemical Reagent Co. Ltd. All chemicals were of analysis of pure and used without further purification.

2.2. Fabrication of samples

2.2.1. Synthesis of NH_2-MIL-53(Fe)

The synthesis of NH_2-MIL-53(Fe) was on the basis of a facile solvothermal method according to previous reports with some modification [29,31]. Typically, $FeCl_3{\cdot}6H_2O$ (2 mmol, 540 mg) and NH_2-BDC (2 mmol, 382 mg) were poured into 36 mL DMF solution at ambient temperature and stirred for 1 h. Afterwards, the above solution was added into a Teflon-lined stainless-steel autoclave (50 mL) and heated to 150 ℃ for 24 h. when the temperature was allowed to cool to ambient, the product was obtained by wash with DMF and methanol and centrifugation (10,000 rpm) for 3 min. Finally, the resulting black brown product was dried at 120 ℃ for 12 h under vacuum conditions and ground into powder.

2.2.2. Synthesis of g-C_3N_4

The g-C_3N_4 powders were synthesized via a thermal condensation

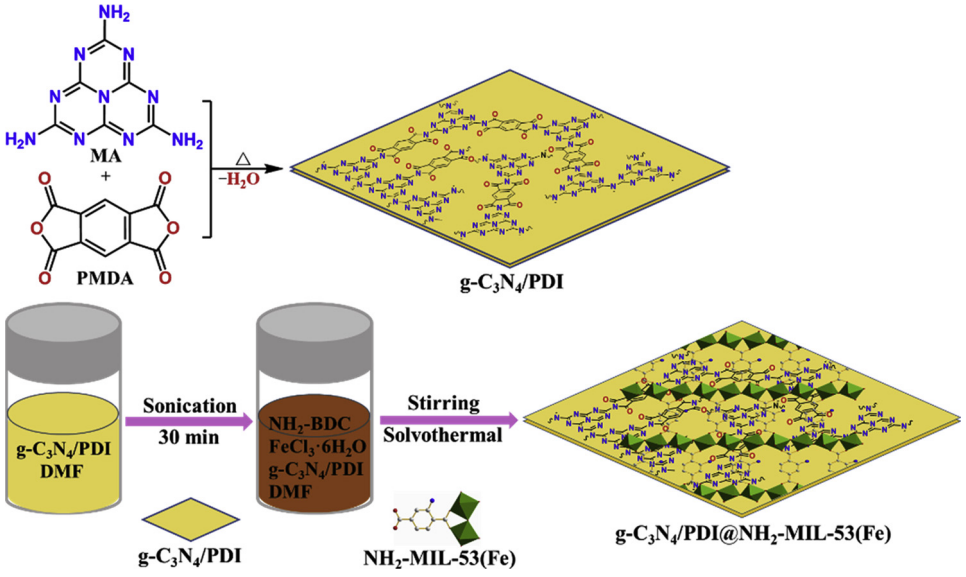

Scheme 1. Schematic illustration of the preparation of the g-C_3N_4/PDI@NH_2-MIL-53(Fe) composite.

process according to the literature [32]. In a typical synthesis, 5 g of melamine calcined at a rate of 5 °C min^{-1} up to 550 °C for 4 h in a muffle furnace under air. The resulting product was obtained as a yellow powder.

2.2.3. Synthesis of MA

Melem (MA) was fabricated following reported procedures [14]. Briefly, 5 g of melamine was added into an alumina crucible with a cover and calcined at a rate of 7 °C min^{-1} up to 425 °C for 4 h in a muffle furnace under air. The resulting product was obtained as a white-beige powder.

2.2.4. Synthesis of g-C_3N_4/PDI

g-C_3N_4/PDI was synthesized using the previously reported route by calcination of a powder mixture of PMDA and MA [16,17,33]. PMDA (10 mmol) and MA (10 mmol) were mixed evenly by grinding in an agate mortar. Subsequently, the mixture was transferred into a porcelain crucible with a cover and heated at 7 °C min^{-1} up to 325 °C for 4 h. The yellow product was ground into powder, and the unreacted monomers were removed by washing with water three times at 50 °C. Finally, the yellow power was filtered and dried at 100 °C for 12 h under vacuum.

2.2.5. Synthesis of g-C_3N_4/PDI@NH_2-MIL-53(Fe)

The preparation of g-C_3N_4/PDI@NH_2-MIL-53(Fe) is depicted in Scheme 1. These composites consisting of different g-C_3N_4/PDI vs NH_2-MIL-53(Fe) ratios were prepared via a facile hydrothermal process. Firstly, an appropriate amount of g-C_3N_4/PDI powder was dispersed into 36 mL DMF by ultrasonication for 30 min. Then, $FeCl_3{\cdot}6H_2O$ (2 mmol, 540 mg) and NH_2-BDC (2 mmol, 382 mg) were added to the suspension with vigorous stirring for 60 min. Afterwards, the solution was transferred to a Teflon-lined stainless-steel autoclave (50 mL), and heated at 150 ℃ for 24 h. The remainder of the procedure is similar to that for the preparation of NH_2-MIL-53(Fe). The resultant products were named CPM-1, CPM-2, CPM-3, with the weight content of the g-C_3N_4/PDI being 25%, 50% and 75%, respectively.

2.3. Characterization

Power X-ray diffraction (PXRD) of the samples were measured using an X'Pert-Pro MPD to analysis the crystallographic structure of the materials. Fourier transform infrared (FT-IR) spectra were collected on a Nicolet 4700 spectrometer. Thermogravimetric Analysis (TGA) were conducted on a TA dynamic TGA 2960 instrument, rising from ambient temperature to 800 °C and an air flow rate of 50 mL/min at a heating rate of 10 °C/min. Scanning electron microscopy (SEM, Hitachi S-4800) coupled with energy-dispersive X-ray (EDX), transmission electron microscopy (TEM, Hitachi H600, 200 kV), and high angle annular dark field scanning transmission electron microscopy coupled with energy-dispersive X-ray (HAADF-STEM, FEI Tecnai F-20) were utilized to observe the morphology, size and elemental distribution of the material. X-ray photoelectron spectroscopy of the as-prepared samples were analyzed on an X-ray photoelectron spectrometer (XPS, ESCALAB MK II). The binding energies were calibrated by using adventitious carbon contamination (C (1 s) = 284.8 eV) as a charge reference. The UV–vis diffuse reflectance spectra (UV–vis DRS) were collected on a CARY 50 spectrometer equipped with integrating sphere. A fluorescence spectrophotometer (FLS920) was employed to measure the photoluminescence (PL) spectra of the samples with an excitation wavelength of 370 nm. The signals of •OH was detected by electron spin-resonance spectroscopy (ESR, JES-X320), 50 mM DMPO aqueous solution was used as a paramagnetic species spin-trap agent. The photocurrent spectra were recorded on a CHI 660B electrochemical system (Shanghai, China) equipped with three standard electrodes: Pt as the counter electrode and Ag/AgCl as the reference electrode, the sample as the working electrode, and Na_2SO_4 (0.01 M) as the electrolyte [34]. 5 mg of sample powder were dispersed in 5 mL of deionized water by sonication. The suspension was cover onto the surface of indium-tin oxide (ITO) glass and dried under an infrared baking lamp to obtain the working electrode. A Xenon lamp (300 W) was used to simulate sunlight.

2.4. Photocatalytic experiments

The photocatalytic activity of g-C_3N_4/PDI@NH_2-MIL-53(Fe) was tested by the photocatalytic degradation of organic pollutants using a PCX50 A Discover multichannel photocatalytic reaction system with a LED white lamp (380–800 nm, 5 W) as a source of visible light **(Fig. S1)**, as reported in our previous work [35]. A certain amount of photocatalyst was added to 50 mL target waste water under magnetic stirring (500 rpm). First, the solution was keep in the dark with stirring for 1.5 h to realize the saturation adsorption. Subsequently, a certain amount of H_2O_2 was added to the mixture and the LED lamp was turned on. Afterwards, 3 mL samples were periodically collected and filtered through a 0.22 μm syringe filter to remove the solid photocatalyst. Finally, the concentration of the samples was determined using a UV–vis spectrometer or HPLC. To estimate the stability and reusability of the photocatalyst, the experiments were conducted over five consecutive cycles using the recycled catalyst. After each reaction, the solid photocatalyst was collected by centrifugation, and thoroughly washed with ultrapure water and ethanol for the next test.

2.5. Analytical methods

The remaining concentrations of TC and CBZ were measured with a UV–vis spectrometer at a maximum absorption wavelength of 357 nm and 285 nm, respectively. High-pressure liquid chromatography (HPLC, Agilent 1260, USA) using a Thermo Syncronics C18 column (250 mm × 4.6 mm, 5 μm) with a UV–Vis detector was used to detect the concentrations of BPA and PNP in solution. The concentrations of BPA and PNP were measured at their maximum absorption wavelength of 278 nm and 320 nm, respectively. 70% methanol and 30% ultrapure water was used as the mobile phase at a flow rate of 0.7 mL/min. The HPLC spectra obtained for the photocatalytic degradation process are provided in the supporting information.

3. Results and discussion

3.1. Characterization of the photocatalysts CPM

Powder-XRD patterns of the as-prepared NH_2-MIL-53(Fe), g-C_3N_4/PDI and CPM photocatalysts are shown in Fig. 1. The XRD patterns of MA and g-C_3N_4 are presented in **Fig. S2a**. The crystallographic features of MA and g-C_3N_4 are in agreement with that reported in the literature

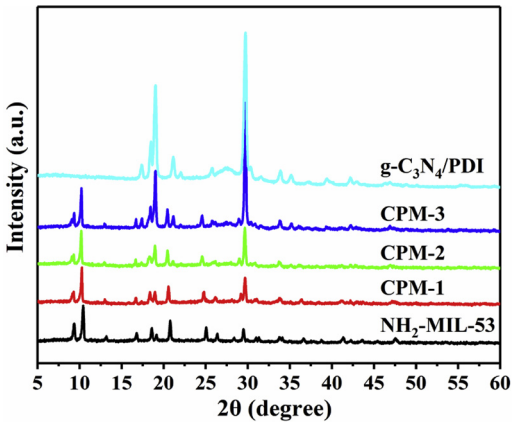

Fig. 1. XRD patterns of NH_2-MIL-53(Fe), g-C_3N_4/PDI and CPM composites.

[14,36]. The diffraction peaks of g-C_3N_4/PDI and NH_2-MIL-53(Fe) are well-matched with previously reported NH_2-MIL-53(Fe) and g-C_3N_4/PDI [17,37], indicating that both photocatalysts were successfully prepared. Interestingly, the XRD patterns of the CPM composites are similar to that of NH_2-MIL-53(Fe), implying that the crystal structure of NH_2-MIL-53(Fe) is well-preserved after being anchored onto the g-C_3N_4/PDI sheets. Additionally, there are two new obvious characteristic diffraction peaks at $2\theta = 19.0^\circ$ ($d = 0.467$ nm) and 29.6°($d = 0.302$ nm) present in the XRD patterns of the CPM hybrids, which correspond to π-π stacking of the PDI units and donor–acceptor interaction between the melem and PDI units [17], respectively. It can be observed that the characteristic peak of g-C_3N_4/PDI gradually becomes more obvious following an increase in the ratio of g-C_3N_4/PDI in the CPM composites. Afterwards, the thermal stability of these photocatalysts was also measured by thermogravimetric analysis (**Fig. S2b**). The initial weight loss before 100 °C can be ascribed to the departure of the guest solvent from the MOF framework. The decomposition temperature of CPM is 260 °C, the same as that of NH_2-MIL-53(Fe), and the corresponding decomposition product is Fe_2O_3. Moreover, the residual percentage of CPM gradually decreases with increasing g-C_3N_4/PDI content, in agreement with the weight content of the g-C_3N_4/PDI. In fact, the residual percentage of CPM-2 is smaller than that of the Fe-MOF, because the release of the guest methanol molecules from the channels of the MOF in Fe-MOF is much higher than CPM-2 at temperatures between 25 and 100 °C.

The FT-IR spectra of the as-synthesized samples is shown in Fig. 2. In comparison, the FT-IR spectra of the CPM composites are similar to the pure NH_2-MIL-53(Fe), indicating that the NH_2-MIL-53(Fe) framework has been successfully synthesized into the CPM composites [16,38]. The absorption peak corresponding to the stretching vibration of the C—N—C bonds in the pentahedral imide shifted slightly in the CPM composites compared with g-C_3N_4/PDI (1373 cm^{-1}), thus suggesting there is an interaction between g-C_3N_4/PDI and NH_2-MIL-53(Fe) [39–41]. The peaks at 1772, 1716 and 726 cm^{-1} correspond to asymmetric secondary shrinkage, symmetrical stretching and the bending vibration absorption peak of the C═O group, respectively, in the five-membered imide ring; these peaks become more evident with the increasing percentage of g-C_3N_4/PDI in CPM composites. These results further confirm that g-C_3N_4/PDI is hybridized successfully with the Fe-MOF.

The morphologies of the as-synthesized materials were analyzed by SEM and TEM, as presented in Fig. 3. Massive laminates formed by stacking are observed on the pristine g-C_3N_4/PDI (Fig. 3**a and b**), in agreement with those reported previously [33,40]. The SEM and TEM images of CPM-2 reveal that the spindle-shaped NH_2-MIL-53(Fe) are in close contact with the surface of the g-C_3N_4/PDI [22], as shown in Fig. 3**c** and **d**. The TEM image (marked by the yellow rectangle in Fig. 3d) and STEM EDX mapping (**Fig. S3**) of CPM-2 at high-magnification clearly show an interface contact between the MOF particles and g-C_3N_4/PDI layer [40,41]. This close contact is beneficial to the transmission of interface electron [42]. Fig. 4 shows the SEM and elemental mapping images of CPM-2. From these images, it can be seen that the elements C, N, O and Fe are well-distributed throughout CPM-2, indicating that the Fe-MOF has grown well on the surface of g-C_3N_4/PDI.

The chemical environment and elemental composition of the as-synthesized products were investigated by XPS analysis. As shown in Fig. 5a, the survey scanning spectrum testify the existence of C, O, N and Fe in CPM-2. In comparison, the intensity of N in CPM-2 is stronger than that in NH_2-MIL-53(Fe), suggesting the successful hybridization of g-C_3N_4/PDI and Fe-MOF. The C1 s spectrum of CPM-2 illustrated in Fig. 5b, shows four peaks at 284.8, 285.8, 288.3 and 289.0 eV. Specifically, the peaks at 284.8, 285.8 and 289.0 eV can be assigned to aromatic carbons, C—N or C—O and C═O of g-C_3N_4/PDI or NH_2-MIL-53(Fe) [43–45], respectively. The rest one peak at 288.3 eV can be attributed to C-$(N)_3$ group from melem units of g-C_3N_4/PDI [46]. Fig. 5**c** illustrates the N 1s spectra of CPM-2. The four characteristic peaks located at 398.7, 399.4, 400.2 and 401.2 eV, can be attributed to C═N—C, C—N, N—$(C)_3$ and N—H [17,43]. For the N 1 s spectra of NH_2-MIL-53(Fe), two obvious peaks located at 399.3 and 400.4 eV can be assigned to the C—N and N—H of the NH_2-BDC linker [47]. Compared with pristine g-C_3N_4/PDI, the peaks of C═N—C and C—N of CPM-2 show a slight positive shift, which may be due to the interaction of Fe^{3+} with the vicinal N atom, causing a decrease in the electron density of C—N or C═N bonds [46]. Furthermore, the Fe 2p spectra of CPM-2 was also analyzed, as shown in Fig. 5**d**. The binding energies at 712.1 and 725.7 eV with a satellite signal at 715.8 eV confirm the presence of Fe^{3+} in the CPM-2 structure [29,31]. Compared with NH_2-MIL-53(Fe), it is worth pointing out that the binding energy of CPM-2 has a negative shift, which can be ascribed to the increased electron density of Fe^{3+} in which the neighboring pyridinic N, possessing a lone pair of electrons in the g-C_3N_4/PDI structure, provide the electron for the Fe^{3+} site in NH_2-MIL-53(Fe) [44,48]. These results further indicate that there is some contact between g-C_3N_4/PDI and MOF, and a heterojunction is formed in the CPM-2 photocatalyst. In addition, the XPS spectra of g-C_3N_4, CPM-1 and CPM-3 are illustrated in **Fig. S4**, and the percentage weight of atoms in the photocatalyst are shown in **Table S1**. The result is substantially consistent with the weight content of the g-C_3N_4/PDI in the CPM added during the synthetic process.

UV − vis DRS spectroscopy was performed to evaluate the optical response of the prepared photocatalysts. The NH_2-MIL-53(Fe) possessed a maximum visible light absorption edge at about 800 nm, as shown in Fig. 6**a**. Compared with that of g-C_3N_4/PDI, the absorption range in the visible region widens following the introduction of Fe-MOF into the g-C_3N_4/PDI. However, the intensity of the absorption peak increases gradually following an increase in Fe-MOF content, as evidenced by NH_2-MIL-53(Fe) with showing stronger absorption in visible light region. Furthermore, the bandgap energies were calculated based on Tauc plots ($(\alpha h\nu)^2 = A(h\nu - E_g)$). The E_g of the pure g-C_3N_4/PDI and NH_2-

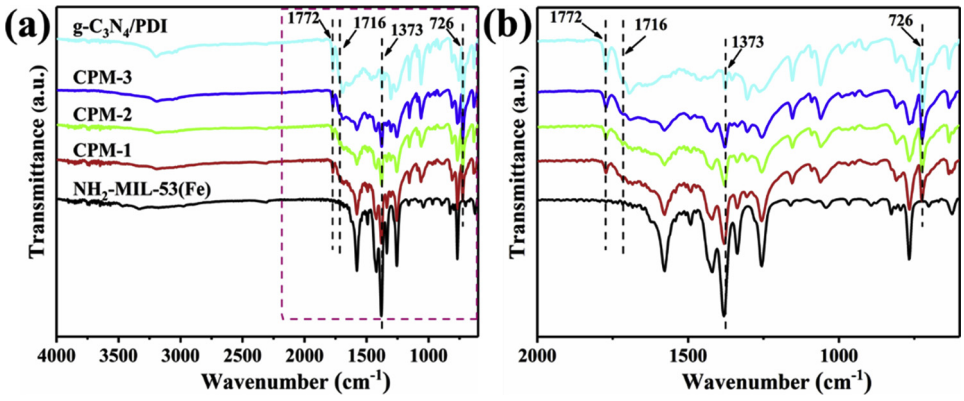

Fig. 2. (a) FT-IR spectra of NH_2-MIL-53(Fe), g-C_3N_4/PDI and CPM composites; (b) High-magnification FT-IR spectra in the rectangle in (a).

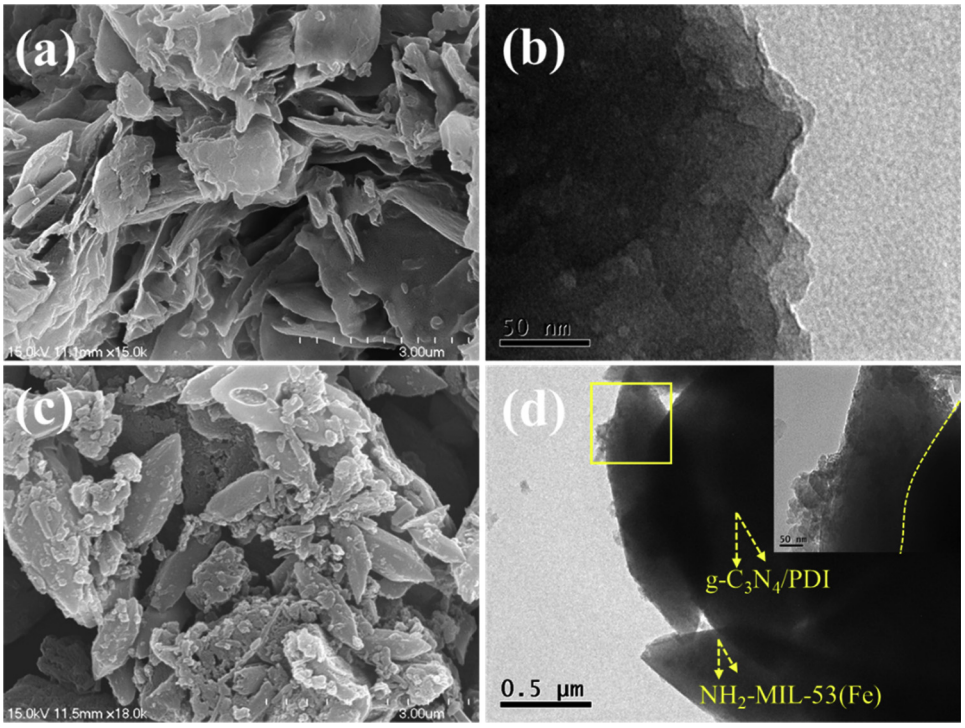

Fig. 3. SEM images of (a) g-C_3N_4/PDI and (c) CPM-2; TEM images of (b) g-C_3N_4/PDI and (d) CPM-2 (inset: enlarged image of the yellow frame). (For interpretation of the references to colour in this figure legend, the reader is referred to the web version of this article).

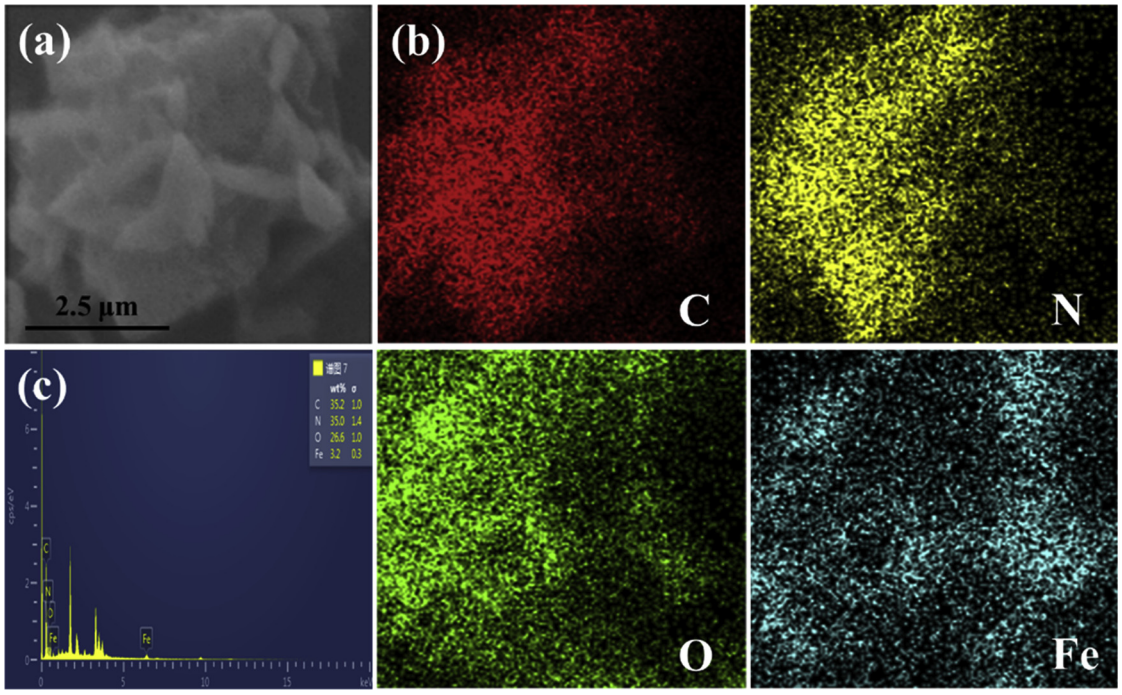

Fig. 4. (a) SEM image of CPM-2, (b) SEM EDX mappings of C, O, N and Fe, and (c) EDS spectrum of CPM-2.

MIL-53(Fe) were estimated to be 1.88 and 2.72 eV, respectively, as shown in Fig. 6b. In contrast, the E_g edge of the CPM narrows with the decreasing weight content of g-C_3N_4/PDI in CPM. The E_g were values were calculated to be 2.11, 2.15 and 2.48 eV, corresponding to CPM-1, CPM-2 and CPM-3, respectively. The results of the optical response indicate that the preparation of the heterostructure g-C_3N_4/PDI@MOF photocatalysts can significantly improve the optical absorption properties and enhance the conversion efficiency of solar light, which is beneficial to enhancing the photocatalytic activity.

The transfer of photogenerated electrons between NH_2-MIL-53 and g-C_3N_4/PDI was investigated by PL analysis. Fig. 7**a** displays the PL spectra of g-C_3N_4/PDI and CPM, and Fig. 7**b** is the enlarged image of Fig. 7**a**. The powder of g-C_3N_4/PDI showed strong photoluminescence behavior, since g-C_3N_4/PDI can be excited by ultraviolet light which gives rise to a rapid recombination of photo-generated electron-hole pairs. In comparison, the photoluminescence intensity of the CPM is quenched dramatically, indicating that the recombination of the photogenerated carrier is suppressed after the hybridization of NH_2-MIL-

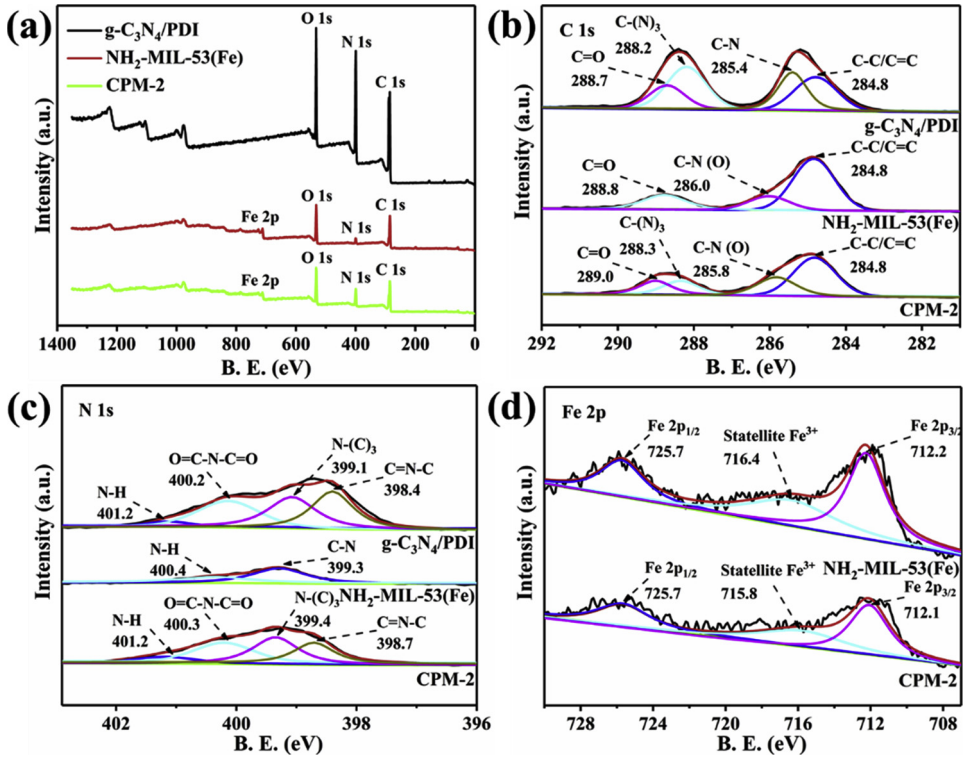

Fig. 5. XPS spectra of NH_2-MIL-53(Fe), CPM-2 and g-C_3N_4/PDI: (a) survey scan, (b) C 1s, (c) N 1s, and (d) Fe 2p.

53(Fe) with g-C_3N_4/PDI. In other words, the NH_2-MIL-53(Fe) sections in the CPM composites facilitate the separation of photo-generated electron-hole pairs from the g-C_3N_4/PDI, resulting in a greater decomposition of H_2O_2 to form ˙OH. As shown in Fig. 7b, the PL intensity of different CPMs decreased obviously compared to g-C_3N_4/PDI. This result further confirms the formation of the heterojunction between NH_2-MIL-53(Fe) and g-C_3N_4/PDI, which can facilitate the transfer of the photon-induced carriers. Moreover, CPM-1 has a weaker PL intensity compared with CPM-2 but lower photocatalytic activity, suggesting that the appropriate loading of g-C_3N_4/PDI in the CPM composites is required to obtain optimal light absorption and the transfer of photo-induced electrons.

To further confirm the formation of a heterojunction between g-C_3N_4/PDI and NH_2-MIL-53(Fe), the photocurrents were measured to determine the separation rate of the photo-generated electron-hole pairs. As shown in Fig. 7c, the current density follows the order: CPM-2 > CPM-1 > NH_2-MIL-53(Fe) > CPM-3 > g-C_3N_4/PDI, indicating that the interfacial charge transfer rate of CPM-2 is faster and so generates more electrons. However, the current density of CPM-2 is slightly unstable, but its photocurrent density is the highest. A similar phenomenon is also observed in other reports [49,50], which may be related to the nature of the material itself. Furthermore, it can be seen that the photocurrent of CPM-3 is slightly lower than that of pristine NH_2-MIL-53(Fe) and is higher than g-C_3N_4/PDI. This decrease may be due to the fact that excessive g-C_3N_4/PDI may shield light absorption, leading to a reduction in the photo-generated electron by NH_2-MIL-53(Fe). It is well known that the photocatalytic activity is influenced by not only the charge separation but also the adsorption of light [44,51]. Thus, a suitable loading of g-C_3N_4/PDI in CPM is necessary to achieve the optimal photocatalytic performance. To further assess the transfer performance of photogenerated charge, the electrochemical impedance of the samples were assessed following the arc radius of the Nyquist impedance plot, as shown in **Fig. S5**. The result matches well with the photocurrent shown in Fig.7**c**. Furthermore, the trend further proves that the appropriate loading of g-C_3N_4/PDI is required; a lower or higher amount of g-C_3N_4/PDI in the CPM composites may cause a slower transfer of photo-induced electrons. This result is also consistent with the PL analysis.

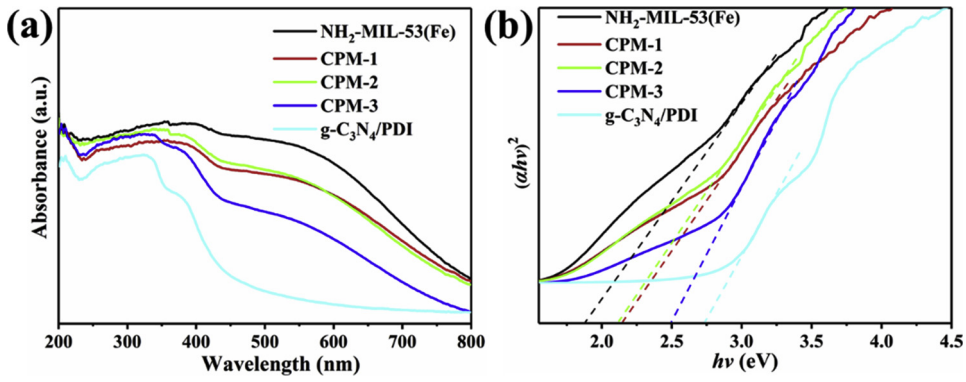

Fig. 6. (a) UV–vis DRS and (b) plot of $(\alpha h\nu)^2$ vs. photon energy ($h\nu$) of the as-synthesized samples.

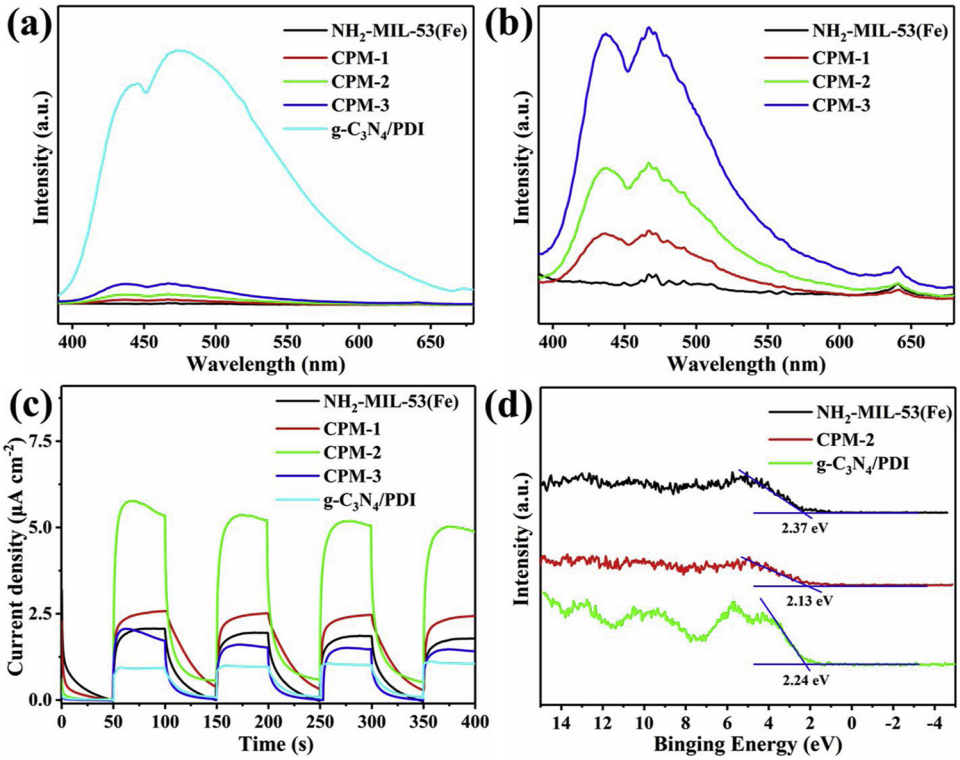

Fig. 7. (a, b) PL spectra (excitation at 370 nm) and (c) photocurrent transient of the photocatalysts, (d) XPS valence band spectra of NH_2-MIL-53, CPM-2 and g-C_3N_4/PDI.

3.2. photocatalytic activity test

The photocatalytic performance of the CPM composites was investigated based on the removal of target pollutants under visible LED light irradiation. First, the photocatalytic treatment of the pharmaceutical micropollutants, TC and CBZ, at low concentration, was conducted with the g-C_3N_4/PDI@NH_2-MIL-53(Fe) photocatalysts. As shown in Fig. 8a, the photocatalytic degradation of TC follows the order CPM-2 > CPM-1 > NH_2-MIL-53(Fe) > g-C_3N_4@NH_2-MIL-53(Fe) > mixed g-C_3N_4/PDI/NH_2- MIL-53(Fe) > CPM-3 > g-C_3N_4/PDI, which is consistent with the photocurrent analysis. More significantly, the TC degradation of the CPM-2 composite reached 90%, which is much higher than that of the parent NH_2-MIL-53(Fe) and g-C_3N_4/PDI, signifying the synergistic effect of the heterojunction formed between NH_2-MIL-53(Fe) and g-C_3N_4/PDI. The excellent photocatalytic capacity of CPM-2 may be due to expedient electron transfer from g-C_3N_4/PDI to NH_2-MIL-53(Fe) and improved light absorption, which can both facilitate the Fenton-like excitation of H_2O_2 to form more ˙OH. Meanwhile,

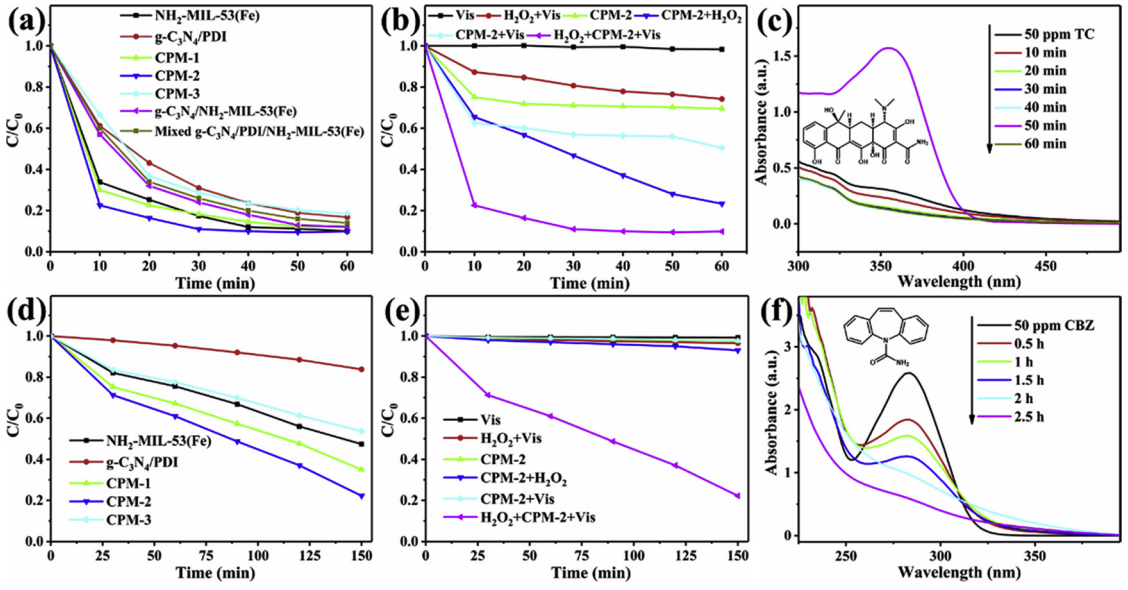

Fig. 8. Photocatalytic degradation of (a) TC using different photocatalysts, (b) different conditions and (c) UV–vis spectra change; photocatalytic degradation of CBZ using (d) different photocatalysts, (e) different conditions and (f) change in UV–vis spectra. (reaction conditions: 0.4 g/L photocatalyst, 10 mM H_2O_2, 50 mL of TC or CBZ at 50 mg/L, pH of 6).

it is worth noting that the photodegradation rate of TC over g-C_3N_4@NH_2-MIL-53(Fe) with 50% of g-C_3N_4 is significantly lower than CPM-2, suggesting the introduction of PDI into g-C_3N_4 improves the photocatalytic performance of the composites. The reason for this phenomenon may be due to the incorporation of the pyromellitic diimides with high electron affinity into the g-C_3N_4/PDI positively shifting the oxidation and reduction potentials, which allows the energy level of NH_2-MIL-53(Fe) to match g-C_3N_4/PDI better than g-C_3N_4 [17,38]. The variation in the UV–vis absorption spectrum of TC over CPM-2 is shown in Fig. 8**c**. For the degradation of CBZ, the order is the same as that of TC, as illustrated in Fig. 8**d**. Compared with parent NH_2-MIL-53(Fe), the photocatalytic performance of the composites is greatly improved, and the highest activity is observed with CPM-2. Fig. 8**f** shows the spectral variation of the UV–vis absorption of CBZ over CPM-2. The photocatalytic efficiency of g-C_3N_4/PDI@NH_2-MIL-53(Fe) is much higher than that of other photocatalysts reported in the literature [52,53].

The effects of different photocatalytic conditions (visible light, H_2O_2 and photocatalyst) on the photocatalytic activity were studied systematically. It can be clearly seen that the degradation efficiencies for TC in the CPM-2/vis, CPM-2/H_2O_2, and CPM-2/H_2O_2/vis systems (Fig. 8b) were 43%, 54% and 90%, respectively, while the degradation efficiencies of CBZ in CPM-2/vis, CPM-2/H_2O_2, and CPM-2/H_2O_2/vis systems (Fig. 8e) were 3%, 7% and 78%, respectively. Moreover, when only visible light was employed in the TC or CBZ solutions, the concentrations of TC and CBZ did not change, suggesting that TC and CBZ are photo-stable in water. A slight degradation of TC and CBZ is observed when H_2O_2 is added, indicating that a combination of visible light and H_2O_2 are able to mildly degrade TC or CBZ in the absence of photocatalyst. It can thus be concluded that both a visible light source and H_2O_2 are essential for improving the degradation efficiency. The results clearly show that the photocatalytic activities for the removal of TC or CBZ are greatly improved using a combination of CPM-2 and H_2O_2 under visible light irradiation.

In order to verify the generality of the photocatalytic behavior of g-C_3N_4/PDI@NH_2-MIL-53(Fe) for the removal of highly toxic phenolic organic pollutants, the photodegradation of BPA and PNP was investigated using CPM-2 under visible light irradiation. Fig. 9**a** and **b** shows the profile for BPA removal; BPA at both a low concentration (50 ppm) and ultralow concentration (2 ppm) can be rapidly degraded within 10 min. Interestingly, the photocatalytic behavior for the degradation of PNP over CPM-2 is similar to that of BPA, as shown in Fig. 9**c** and **d**. These photodegradation behaviors are confirmed by the HPLC spectra shown in **Fig. S6**. These results demonstrate that CPM-2 can be used as an excellent photocatalyst for the rapid removal of toxic phenolic organic pollutants in the presence of visible light. The photocatalytic performance over CPM-2 has been compared to other iron-based photocatalysts. As listed in Table 1, CPM-2 possesses very high photocatalytic activity for the degradation of organic pollutants. This study utilizing the visible LED white light seems to be energy efficient, as well as consuming less energy in the photocatalytic process. Thus, the LED lamp as a source of visible light is more suitable for practical application.

In order to discover the optimal reaction conditions, the effect of the catalyst dosage and H_2O_2 concentration on the photocatalytic activity over CPM-2 was studied. First, the influence of the catalyst concentration for the removal of BPA and PNP was carried out by changing the catalyst loading between 0.1 g/L and 0.4 g/L with a H_2O_2 concentration of 10 mM. The results are shown in **Fig. S7**. The photocatalytic efficiency improves when the catalyst dosage is increased from 0.1 g/L to 0.2 g/L, and then remains nearly constant up to a loading of 0.4 g/L. With regards to the removal of organic pollutants by photo-Fenton oxidation, the optimum catalyst loading has been widely investigated [54]; excessive catalyst dosage leads to competing reactions ($Fe^{2+} + {}^{\cdot}OH \rightarrow Fe^{3+} + OH^{-}$) that reduce the amount of radicals available. Thus, the optimal dose of catalyst found in this work for the removal of BPA and PNP solution (2 mg/L) is 0.2 g/L. Furthermore, the influence of H_2O_2 concentration, in the range 5–20 mM, was further explored with a catalyst dosage of 0.2 g/L. As illustrated in **Fig. S8**, the degradation efficiencies for BPA and PNP over CPM-2 increases with increasing catalyst concentration, and reaches a plateau at a H_2O_2

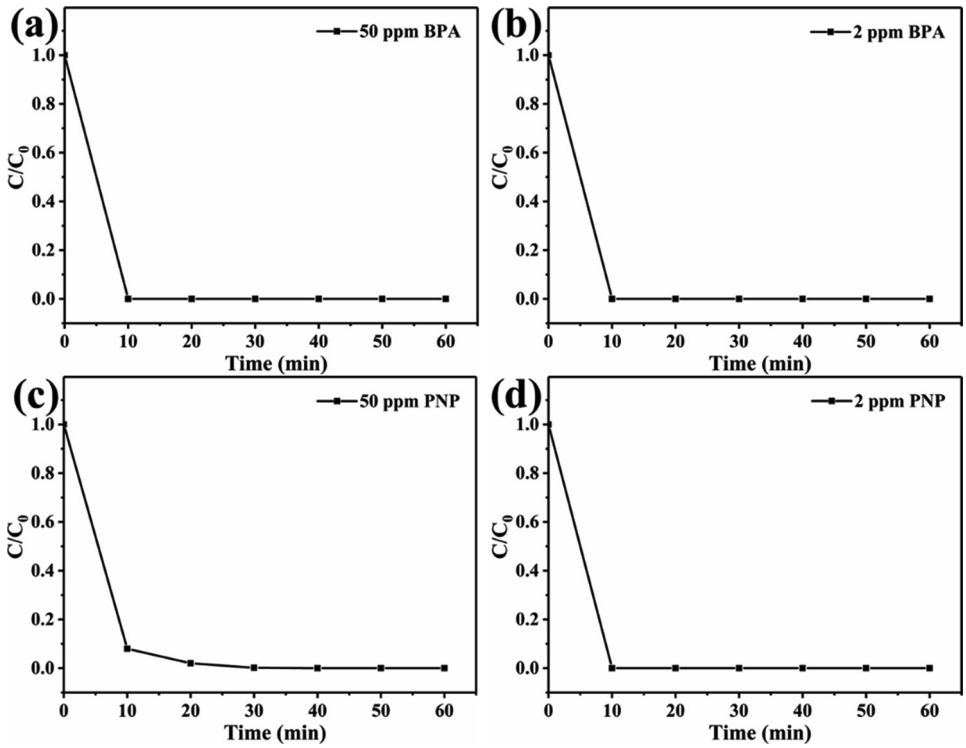

Fig. 9. Photocatalytic degradation of (a) 50 ppm and (b) 2 ppm of BPA; (c) 50 ppm and (d) 2 ppm of PNP over CPM-2. (Reaction condition: 0.4 g/L photocatalyst for BPA or PNP at 50 mg/L and 0.2 g/L photocatalyst for BPA or PNP at 2 mg/L, 10 mM H_2O_2, 50 mL of BPA or PNP, pH of 6).

Table 1
Comparison of the photocatalytic performance of CPM-2 with other Fe-based photocatalysts in the reported literatures under visible light irradiation.

Photocatalysts	Org.	m_{Cat} (g/L)	C_{Org} (ppm)	C_{H2O2} (mM)	t (min)	Con. (%)	Lamp source	ref.
Fe_3O_4@void@TiO_2	TC	0.25	40	377	10	100	Xe lamp (300 w)	[54]
MIL-53(Fe)	CBZ	0.1	40	20	280	90.1	Xe lamp (500 w)	[52]
Ag/AgCl/ferrihydrite	BPA	1	30	10	50	100	LED lamp (5 w)	[55]
Ag/AgBr/ferrihydrite	BPA	1	30	10	60	100	LED lamp (5 w)	[56]
Fe_2O_3/3DOM $BiVO_4$	PNP	0.1	56	60	60	98	Xe lamp (300 w)	[57]
g-C_3N_4/PDI@Fe-MOF	**TC**	**0.4**	**50**	**10**	**60**	**90**	**LED lamp (5 w)**	**this work**
g-C_3N_4/PDI@Fe-MOF	**CBZ**	**0.4**	**50**	**10**	**150**	**78**	**LED lamp (5 w)**	**this work**
g-C_3N_4/PDI@Fe-MOF	**BPA**	**0.4**	**50**	**10**	**10**	**100**	**LED lamp (5 w)**	**this work**
g-C_3N_4/PDI@Fe-MOF	**PNP**	**0.4**	**50**	**10**	**30**	**100**	**LED lamp (5 w)**	**this work**

concentration of 10 mM. Further increasing the H_2O_2 concentration to 20 mM does not cause an obvious improvement in degradation efficiency. Therefore, in consideration of maximum pollutant removal, the optimum H_2O_2 concentration was considered to be 10 mM.

3.3. Stability and recyclability of g-C_3N_4/PDI@NH_2-MIL-53(Fe)

To assess the potential use of the photocatalyst in practical applications, the reusability and long-term stability of the photocatalyst was evaluated. The CPM-2 catalyst was collected by centrifugation and reused in the next test. As illustrated in Fig. 10, the photocatalytic degradation efficiency of TC still reached 80%, even after being used 5 times. The percentage removal of CBZ was slightly lower, with the lowest value being 65%. Significantly, CPM-2 exhibits excellent recyclability for the photocatalytic decomposition of pharmaceutical micropollutants with the irradiation of visible light over five cycles. For phenolic organic pollutants, removal was not significantly affected after five catalytic cycles. Therefore, CPM-2 is stable and can be reused for the removal of pharmaceuticals and phenolic micropollutants, which is important for its practical application.

Furthermore, the structure of CPM-2, after repeated treatment with TC, was fully determined by XRD, FT-IR, SEM, TEM and XPS. As shown in Fig. 11a, the XRD peaks are identical both before and after the reactions, indicating that the structure of the photocatalyst remains mostly unaltered. In terms of the FT-IR spectrum (Fig. 11b), no obvious variation is observed, suggesting that the functional groups are not affected during the photodegradation process. It can be seen from **Fig. S9**, the SEM, TEM images and XPS spectra of the CPM-2 composite after photocatalytic degradation, no significant change occurs in the morphology and chemical environment. Considering the above results, the CPM-2 composite is stable and can be reused multiple times, providing the potential for use in water remediation.

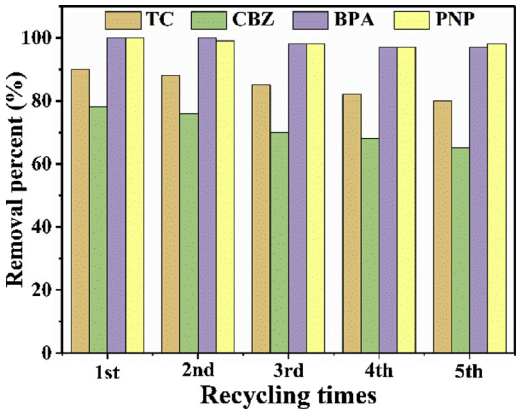

Fig. 10. Recycling test on the removal of TC, CBZ, BPA and PNP. (Reaction condition: 0.4 g/L photocatalyst, 10 mM H_2O_2, 50 mL of wastewater at 50 mg/L, pH of 6).

3.4. Effect of ion species on photocatalytic efficiency

It is well known that inorganic cations and anions such as Ca^{2+}, K^+, Mg^{2+}, Na^+, Cl^-, SO_4^{2-}, NO_3^- and HCO_3^- are common in surface water, groundwater and wastewater, coexisting with the target organic pollutant to be eliminated [58]. For the practical application of photocatalysis in water remediation, the effects of inorganic salts on the photocatalytic performance of the photocatalyst for the removal of target pollutants must be assessed [59]. As shown in Fig. 12a, cations (Ca^{2+}, K^+, Mg^{2+} and Na^+) at 2.5 mM exhibit no appreciably different impacts on the degradation rate of TC. However, a detrimental effect is observed when the photocatalytic reaction is conducted with a high concentration of Cl^- (5 and 10 mM). The inhibitive effect can be attributed to excessively produced ˙Cl from the oxidation of Cl^- by ˙OH, which are less reactive than ˙OH [60,61]. Interestingly, SO_4^{2-} shows a positive effect on the degradation efficiency of TC, as shown in Fig. 12**b**. The enhancement of the TC degradation rate might be due to the synergistic effect between ˙OH and ˙SO_4-, formed from the oxidation of SO_4^{2-} by ˙OH [62–64]. The NO_3- exhibits hardly any effect on the degradation process of TC (Fig. 12c) when its concentration is increased from 2.5 to 10 mM. However, an obviously adverse effect can be observed when HCO_3^- is added into the reaction, as illustrated in Fig. 12**d.** The degradation rate of TC decrease gradually as the concentration of HCO_3^- is increased. The reason for the decrease in degradation rate of TC may be due to HCO_3^- being vulnerable to oxidation by ˙HO, leading to the formation of ˙HCO_3/˙CO_3- at a relatively higher second-order constant of 3.9×10^8 M^{-1} S^{-1} [65]. It has been reported that HCO_3˙/CO_3˙- reacts mostly with electron-rich compounds and is less reactive than ˙HO or ˙SO_4- [63,66].

3.5. Speculated photocatalytic mechanism

In order to determine the main reactive species present in the photocatalytic cycle, tert-butyl alcohol (˙OH scavengers) and p-benzoquinone (˙O_2^- scavenger) were used as scavengers in the photo-Fenton system. The removal efficiency of TC decreases significantly when TBA is added, as illustrated in Fig. 13**a**. Furthermore, the TC removal efficiency decreases slightly following the addition of p-benzoquinone, suggesting that ˙O_2^- is not the directly reactive species in the CPM-2/H_2O_2/Vis system. Therefore, the presence of excess TBA decreases the rate of photocatalytic degradation of TC, indicating that ˙OH is the main reactive species for the degradation of TC in the photo-Fenton-like system. In addition, the presence of ˙OH in the CPM-2/H_2O_2/Vis system was determined by electron spin resonance (ESR), as shown in Fig. 13**b**. An intensity ratio of 1:2:2:1 represents the four characteristic peaks of the DMPO-˙OH species; the CPM-2 has the strongest characteristic quartet peaks, suggesting the amount of generated ˙OH is high [54]. The results further demonstrate that CPM-2 possesses high photocatalytic activity.

To illustrate the possible photocatalytic mechanism of the CPM-2 system, valence band XPS analysis was carried out to measure the band positions. As shown in Fig. 7d, the valence band (VB) positions of NH_2-

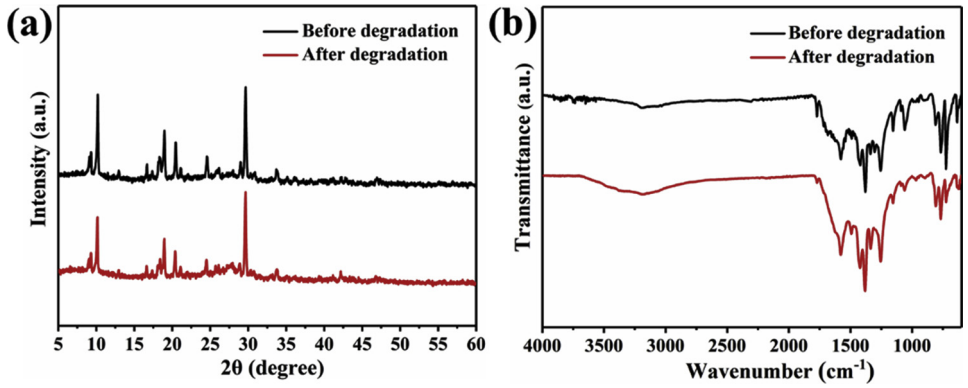

Fig. 11. (a) XRD patterns and (b) FT-IR spectra of CPM-2 composite before and after the photocatalytic degradation.

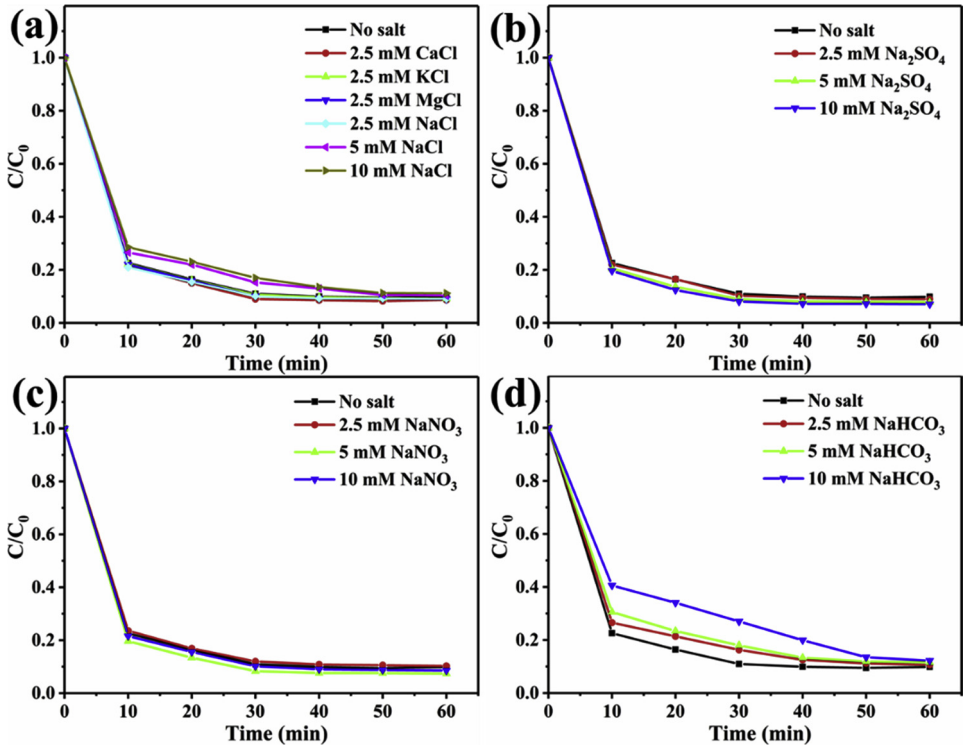

Fig. 12. Effect of common cations and anions on the photocatalytic degradation of TC by CPM-2: (a) Ca^{2+}, K^{+}, Mg^{2+}, Na^{+} and Cl^{-}, (b) SO_4^{2-}, (c) NO_3^{-} and (d) HCO_3- (reaction condition: 0.4 g/L photocatalyst, 10 mM H_2O_2, 50 mL of TC at 50 mg/L, pH of 6).

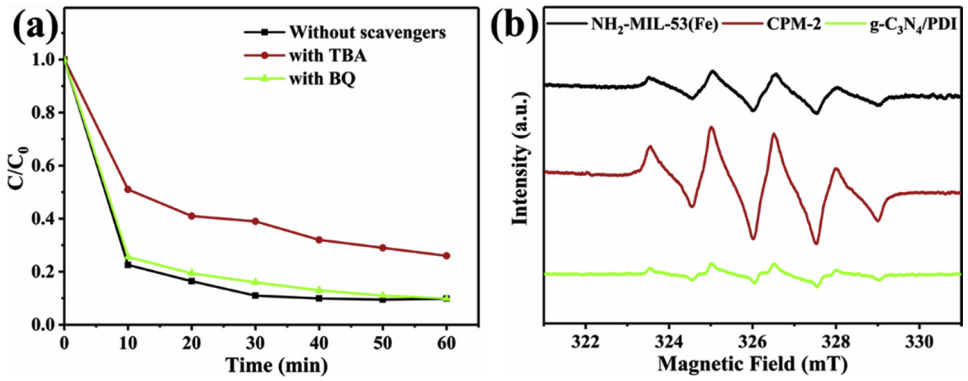

Fig. 13. (a) Effect of different scavengers on the photocatalytic degradation of TC by CPM-2 (reaction condition: 0.4 g/L photocatalyst, 10 mM H_2O_2, 50 mL of TC at 50 mg/L, pH of 6); (b) ESR spectra of CPM-2/H_2O_2 recorded at ambient temperature in aqueous dispersion for DMPO-•OH with the assistance of visible light.

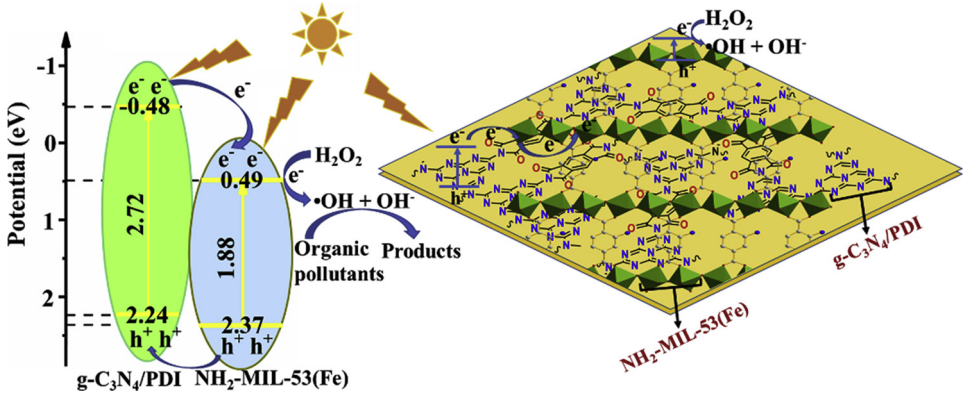

Scheme 2. Schematic illustration for the possible photocatalytic mechanism of the CPM-2 composite under visible light irradiation.

MIL-53(Fe), g-C_3N_4/PDI and CPM-2 were estimated to be 2.37, 2.24 and 2.13 eV vs NHE, respectively. The calculated band gaps of NH_2-MIL-53(Fe), g-C_3N_4/PDI and CPM-2 are 1.88, 2.72 and 2.15 eV vs NHE, respectively, determined from UV-DRS spectroscopy in Fig. 6**b**. The conductance band (CB) position (E_{CB}) of CPM-2 is estimated to be -0.02 eV vs NHE based on the empirical formula of $Eg = E_{VB} - E_{CB}$. The E_{CB} of NH_2-MIL-53(Fe) and g-C_3N_4/PDI is 0.49 and -0.48 eV vs NHE, respectively.

On the basis of the analysis of VB XPS, UV–vis DRS, PL and photocurrent, we propose a possible mechanism for the photocatalytic degradation of organic pollutants in the CPM-2/Visible light/H_2O_2 reaction system. A schematic illustration of the photo-generated e^--h^+ and charge transfer process in the CPM-2 composite is shown in Scheme 2. First, the e^--h^+ pairs can be generated on the -NH_2 group, Fe_3-μ_3-oxo clusters and melem units with the assistance of visible light. Then, the photo-induced electrons from the CB of g-C_3N_4/PDI are transferred to the CB of NH_2-MIL-53(Fe), and the holes from the VB of NH_2-MIL-53(Fe) are transferred to the VB of g-C_3N_4/PDI, which reduces charge recombination and results in more free electrons in the CB of NH_2-MIL-53(Fe). Finally, the Fe^{2+} obtained from reduction of Fe^{3+} by electrons can excite the decomposition of H_2O_2 to form •OH for the oxidation of the organic pollutants. In the photocatalytic system, PDI has a high electron affinity and positively shifts the oxidation and reduction potentials of g-C_3N_4, which allows for electric band structure matching between g-C_3N_4/PDI and NH_2-MIL-53(Fe) [17]. The matching contributes to the efficient formation of the heterojunction, facilitating the fast transfer and separation of photo-induced electron and hole pairs. More importantly, the formation of ˙OH from the excitation of H_2O_2 with the help of Fe^{2+} in NH_2-MIL-53(Fe), is much easier than that of using an electron from g-C_3N_4/PDI with the assistance of visible light [67]. As a result, the efficient formation of heterojunction between g-C_3N_4/PDI and NH_2-MIL-53(Fe) are favorable to enhance the visible light-induced Fenton-like degradation of organic pollutants. The following reaction equations have been proposed:

g-C3N4/PDI + hv → h+ (g-C3N4/PDI) + e- (g-C3N4/PDI)

NH2-MIL-53(Fe) + hv → h+ (NH2-MIL-53(Fe)) + e- (NH2-MIL-53(Fe))

e- (g-C3N4/PDI) + NH2-MIL-53(Fe) → e- (NH2-MIL-53(Fe)) + g-C3N4/PDI

Fe3+ + e- (NH2-MIL-53(Fe)) → Fe2+

Fe2+ + H2O2 → Fe3+ + ˙OH + OH− (k ≈ 70 M-1 S-1)

Fe3+ + H2O2 → Fe2+ + ˙OOH + H+ (k ≈ 0.001-0.01 M-1 S-1)

H2O2 + e- → OH- + ˙OH

˙OH + Organic pollutants → products

4. Conclusion

In summary, thermal condensation, surface growth technology and solvothermal methods were exploited for the preparation of a novel g-C_3N_4/PDI@NH_2-MIL-53(Fe) heterostructure. All of the prepared CPM composites displayed excellent photocatalytic activity towards the pharmaceutical and phenolic micropollutants under visible LED light irradiation. CPM-2 (50%) in particular exhibited excellent efficiency for the removal of the aforementioned organic pollutants (90% TC, 78% CBZ, 100% BPA and 100% PNP). Furthermore, very low concentrations of organic pollutants (2 ppm of BPA or PNP) could also be efficiently removed with CPM-2 within 10 min. The improvement in the photo-Fenton-like performance can be attributed to the wide visible light adsorption region and the efficient formation of heterojunction derived from the interface contact and energy level matching between g-C_3N_4/PDI and NH_2-MIL-53(Fe). Repeated experimental studies and structural analysis demonstrated that CPM-2 was stable and can be reused multiple times. The findings of this work demonstrate that metal-free semiconductor and MOF composites have the potential for use in the removal of organic pollutants for water remediation.

Acknowledgments

This work was supported by the National Natural Science Foundation of China (21776190, 21336005, 51773144) and PAPD in Jiangsu Province.

Appendix A. Supplementary data

Supplementary material related to this article can be found, in the online version, at doi:https://doi.org/10.1016/j.apcatb.2019.03.024.

References

[1] M.A. Ashraf, Persistent organic pollutants (POPs): a global issue, a global challenge, Environ. Sci. Pollut. Res. Int. 24 (2017) 4223–4227.
[2] Q. Zheng, H.J. Lee, J. Lee, W. Choi, N.B. Park, C. Lee, Electrochromic titania nanotube arrays for the enhanced photocatalytic degradation of phenol and pharmaceutical compounds, Chem. Eng. J. 249 (2014) 285–292.
[3] J.L. Zhao, G.G. Ying, L. Wang, J.F. Yang, X.B. Yang, L.H. Yang, X. Li, Determination of phenolic endocrine disrupting chemicals and acidic pharmaceuticals in surface water of the Pearl Rivers in South China by gas chromatography-negative chemical ionization-mass spectrometry, Sci. Total Environ. 407 (2009) 962–974.
[4] J.M. Herrmann, Heterogeneous photocatalysis: fundamentals and applications to the removal of various types of aqueous pollutants, Catal. Today 53 (1999) 115–129.
[5] R.A. Torres, J.I. Nieto, E. Combet, C. Pétrier, C. Pulgarin, Influence of TiO_2 concentration on the synergistic effect between photocatalysis and high-frequency ultrasound for organic pollutant mineralization in water, Appl. Catal. B: Environ. 80 (2008) 168–175.

[6] V. Vaiano, M. Matarangolo, J.J. Murcia, H. Rojas, J.A. Navío, M.C. Hidalgo, Enhanced photocatalytic removal of phenol from aqueous solutions using ZnO modified with Ag, Appl. Catal. B: Environ. 225 (2018) 197–206.

[7] X.J. Wen, C. Zhang, C.G. Niu, L. Zhang, G.M. Zeng, X.G. Zhang, Highly enhanced visible light photocatalytic activity of CeO_2 through fabricating a novel p–n junction $BiOBr/CeO_2$, Catal. Commun. 90 (2017) 51–55.

[8] J.L. Yang, J. Xu, H. Ren, L. Sun, Q.C. Xu, H. Zhang, J.F. Li, Z.Q. Tian, In situ SERS study of surface plasmon resonance enhanced photocatalytic reactions using bifunctional Au@CdS core-shell nanocomposites, Nanoscale 9 (2017) 6254–6258.

[9] X. Wang, K. Maeda, A. Thomas, K. Takanabe, G. Xin, J.M. Carlsson, K. Domen, M. Antonietti, A metal-free polymeric photocatalyst for hydrogen production from water under visible light, Nat. Mater. 8 (2009) 76–80.

[10] Y. Zheng, J. Liu, J. Liang, M. Jaroniec, S.Z. Qiao, Graphitic carbon nitride materials: controllable synthesis and applications in fuel cells and photocatalysis, Energy Environ. Sci. 5 (2012) 6717.

[11] G. Mamba, A.K. Mishra, Graphitic carbon nitride ($g\text{-}C_3N_4$) nanocomposites: A new and exciting generation of visible light driven photocatalysts for environmental pollution remediation, Appl. Catal. B: Environ. 198 (2016) 347–377.

[12] D. Masih, Y. Ma, S. Rohani, Graphitic C3N4based noble-metal-free photocatalyst systems: a review, Appl. Catal. B: Environ. 206 (2017) 556–588.

[13] Z. Zhao, Y. Sun, F. Dong, Graphitic carbon nitride based nanocomposites: a review, Nanoscale 7 (2015) 15–37.

[14] S. Chu, C. Wang, J. Feng, Y. Wang, Z. Zou, Melem: a metal-free unit for photocatalytic hydrogen evolution, Int. J. Hydrogen Energ. 39 (2014) 13519–13526.

[15] H. Yu, R. Shi, Y. Zhao, T. Bian, Y. Zhao, C. Zhou, G.I.N. Waterhouse, L.Z. Wu, C.H. Tung, T. Zhang, Alkali-assisted synthesis of nitrogen deficient graphitic carbon nitride with tunable band structures for efficient visible-light-driven hydrogen evolution, Adv. Mater. (2017) 29.

[16] S. Chu, Y. Wang, Y. Guo, J. Feng, C. Wang, W. Luo, X. Fan, Z. Zou, Band structure engineering of carbon nitride: in search of a polymer photocatalyst with high photooxidation property, ACS Catal. 3 (2013) 912–919.

[17] Y. Shiraishi, S. Kanazawa, Y. Kofuji, H. Sakamoto, S. Ichikawa, S. Tanaka, T. Hirai, Sunlight-driven hydrogen peroxide production from water and molecular oxygen by metal-free photocatalysts, Angew. Chem. Int. Ed. 53 (2014) 13454–13459.

[18] I.W. Hwang, C. Soci, D. Moses, Z. Zhu, D. Waller, R. Gaudiana, C.J. Brabec, A.J. Heeger, Ultrafast electron transfer and decay dynamics in a small band gap bulk heterojunction material, Adv. Mater. 19 (2007) 2307–2312.

[19] L. Sun, Y. Qi, C.J. Jia, Z. Jin, W. Fan, Enhanced visible-light photocatalytic activity of $g\text{-}C_3N_4/Zn_2GeO_4$ heterojunctions with effective interfaces based on band match, Nanoscale 6 (2014) 2649–2659.

[20] L. Zeng, X. Guo, C. He, C. Duan, Metal – organic frameworks: versatile materials for heterogeneous photocatalysis, ACS Catal. 6 (2016) 7935–7947.

[21] C. Wang, X. Liu, N. Keser Demir, J.P. Chen, K. Li, Applications of water stable metal-organic frameworks, Chem. Soc. Rev. 45 (2016) 5107–5134.

[22] W. Huang, N. Liu, X. Zhang, M. Wu, L. Tang, Metal organic framework $g\text{-}C_3N_4$ /MIL-53(Fe) heterojunctions with enhanced photocatalytic activity for Cr(VI) reduction under visible light, Appl. Surf. Sci. 425 (2017) 107–116.

[23] X. Zhang, Y. Yang, W. Huang, Y. Yang, Y. Wang, C. He, N. Liu, M. Wu, L. Tang, $g\text{-}C_3N_4$/UiO-66 nanohybrids with enhanced photocatalytic activities for the oxidation of dye under visible light irradiation, Mater. Res. Bull. 99 (2018) 349–358.

[24] Z.D. Lei, Y.C. Xue, W.Q. Chen, L. Li, W.H. Qiu, Y. Zhang, L. Tang, The influence of carbon nitride nanosheets doping on the crystalline formation of MIL-88B(Fe) and the photocatalytic activities, Small 14 (2018) e1802045.

[25] Y. Zhang, Z. Jin, A. luan, G. Wang, Charge transfer behaviors over MOF-5@$g\text{-}C_3N_4$ with $Ni_xMo_{1-x}S_2$ modification, Int. J. Hydrogen Energy 43 (2018) 9914–9923.

[26] Y. Pan, D. Li, H.L. Jiang, Sodium-doped C_3N_4/MOF heterojunction composites with tunable band structures for photocatalysis: interplay between light harvesting and electron transfer, Chem. Eur. J. 24 (2018) 18403–18407.

[27] K.G. Laurier, F. Vermoortele, R. Ameloot, D.E. De Vos, J. Hofkens, M.B. Roeffaers, Iron(III)-based metal-organic frameworks as visible light photocatalysts, J. Am. Chem. Soc. 135 (2013) 14488–14491.

[28] X. Liu, Y. Zhou, J. Zhang, L. Tang, L. Luo, G. Zeng, Iron containing metal-organic frameworks: structure, synthesis, and applications in environmental remediation, ACS Appl. Mater. Interfaces 9 (2017) 20255–20275.

[29] R. Liang, F. Jing, L. Shen, N. Qin, L. Wu, MIL-53(Fe) as a highly efficient bifunctional photocatalyst for the simultaneous reduction of Cr(VI) and oxidation of dyes, J. Hazard. Mater. 287 (2015) 364–372.

[30] Y. Gao, S. Li, Y. Li, L. Yao, H. Zhang, Accelerated photocatalytic degradation of organic pollutant over metal-organic framework MIL-53(Fe) under visible LED light mediated by persulfate, Appl. Catal. B: Environ. 202 (2017) 165–174.

[31] R. Liang, L. Shen, F. Jing, N. Qin, L. Wu, Preparation of MIL-53(Fe)-reduced graphene oxide nanocomposites by a simple self-assembly strategy for increasing interfacial contact: efficient visible-light photocatalysts, ACS Appl. Mater. Interfaces 7 (2015) 9507–9515.

[32] M. Xu, L. Han, S. Dong, Facile fabrication of highly efficient $g\text{-}C_3N_4/Ag_2O$ heterostructured photocatalysts with enhanced visible-light photocatalytic activity, ACS Appl. Mater. Interfaces 5 (2013) 12533–12540.

[33] Y. Kofuji, Y. Isobe, Y. Shiraishi, H. Sakamoto, S. Tanaka, S. Ichikawa, T. Hirai, Carbon nitride-aromatic diimide-graphene nanohybrids: metal-free photocatalysts for solar-to-hydrogen peroxide energy conversion with 0.2% efficiency, J. Am. Chem. Soc. 138 (2016) 10019–10025.

[34] H. Li, S. Gan, H. Wang, D. Han, L. Niu, Intercorrelated superhybrid of AgBr supported on graphitic-C_3N_4-decorated nitrogen-doped graphene: high engineering photocatalytic activities for water purification and CO_2 reduction, Adv. Mater. 27 (2015) 6906–6913.

[35] Y. Li, J. Jiang, Y. Fang, Z. Cao, D. Chen, N. Li, Q. Xu, J. Lu, TiO_2 Nanoparticles anchored onto the metal–organic framework nh_2-mil-88b(fe) as an adsorptive photocatalyst with enhanced fenton-like degradation of organic pollutants under visible light irradiation, ACS Sustain. Chem. Eng. 6 (2018) 16186–16197.

[36] Y. Shiraishi, S. Kanazawa, Y. Sugano, D. Tsukamoto, H. Sakamoto, S. Ichikawa, T. Hirai, Highly selective production of hydrogen peroxide on graphitic carbon nitride ($g\text{-}C_3N_4$) photocatalyst activated by visible light, ACS Catal. 4 (2014) 774–780.

[37] S. Bauer, C. Serre, T. Devic, P. Horcajada, J. Marrot, G. Férey, N. Stock, High-throughput assisted rationalization of the formation of metal organic frameworks in the iron(III) aminoterephthalate solvothermal system, Inorg. Chem. 47 (2008) 7568–7576.

[38] S. Chu, Y. Wang, Y. Guo, P. Zhou, H. Yu, L. Luo, F. Kong, Z. Zou, Facile green synthesis of crystalline polyimide photocatalyst for hydrogen generation from water, J. Mater. Chem. 22 (2012) 15519.

[39] L. Lin, P. Ye, C. Cao, Q. Jin, G.S. Xu, Y.H. Shen, Y.P. Yuan, Rapid microwave-assisted green production of a crystalline polyimide for enhanced visible-light-induced photocatalytic hydrogen production, J. Mater. Chem. A Mater. Energy Sustain. 3 (2015) 10205–10208.

[40] Q. Guo, H. Li, Q. Zhang, Y. Zhang, Fabrication, characterization and mechanism of a novel Z-scheme Ag_3PO_4/NG/polyimide composite photocatalyst for microcystin-LR degradation, Appl. Catal. B: Environ. 229 (2018) 192–203.

[41] P. Meng, H. Heng, Y. Sun, J. Huang, J. Yang, X. Liu, Positive effects of phosphotungstic acid on the in-situ solid-state polymerization and visible light photocatalytic activity of polyimide-based photocatalyst, Appl. Catal. B: Environ. 226 (2018) 487–498.

[42] P. Meng, H. Heng, Y. Sun, X. Liu, In situ polymerization synthesis of Z-scheme tungsten trioxide/polyimide photocatalyst with enhanced visible-light photocatalytic activity, Appl. Surf. Sci. 428 (2018) 1130–1140.

[43] Y. Kofuji, S. Ohkita, Y. Shiraishi, H. Sakamoto, S. Tanaka, S. Ichikawa, T. Hirai, Graphitic carbon nitride doped with biphenyl diimide: efficient photocatalyst for hydrogen peroxide production from water and molecular oxygen by sunlight, ACS Catal. 6 (2016) 7021–7029.

[44] X. Li, Y. Pi, L. Wu, Q. Xia, J. Wu, Z. Li, J. Xiao, Facilitation of the visible light-induced Fenton-like excitation of H_2O_2 *via* heterojunction of $g\text{-}C_3N_4/NH_2$-Iron terephthalate metal-organic framework for MB degradation, Appl. Catal. B: Environ. 202 (2017) 653–663.

[45] T. Xiao, Z. Tang, Y. Yang, L. Tang, Y. Zhou, Z. Zou, In situ construction of hierarchical $WO_3/g\text{-}C_3N_4$ composite hollow microspheres as a Z-scheme photocatalyst for the degradation of antibiotics, Appl. Catal. B: Environ. 220 (2018) 417–428.

[46] Y. Xu, F. Ge, Z. Chen, S. Huang, W. Wei, M. Xie, H. Xu, H. Li, One-step synthesis of Fe-doped surface-alkalinized $g\text{-}C_3N_4$ and their improved visible-light photocatalytic performance, Appl. Surf. Sci. 469 (2019) 739–746.

[47] L. Shi, T. Wang, H. Zhang, K. Chang, X. Meng, H. Liu, J. Ye, An Amine-functionalized iron(III) Metal-organic framework as efficient visible-light photocatalyst for Cr (VI) reduction, Adv. Sci. 2 (2015) 1500006.

[48] A.J. Wagner, G.M. Wolfe, D.H. Fairbrother, Reactivity of vapor-deposited metal atoms with nitrogen-containing polymers and organic surfaces studied by in situ XPS, Appl. Surf. Sci. 219 (2003) 317–328.

[49] D. Xu, B. Cheng, W. Wang, C. Jiang, J. Yu, $Ag_2CrO_4/g\text{-}C_3N_4$/graphene oxide ternary nanocomposite Z-scheme photocatalyst with enhanced CO_2 reduction activity, Appl. Catal. B: Environ. 231 (2018) 368–380.

[50] H. Wang, Y. Sun, G. Jiang, Y. Zhang, H. Huang, Z. Wu, S.C. Lee, F. Dong, Unraveling the mechanisms of visible light photocatalytic NO purification on earth-abundant insulator-based core-shell heterojunctions, Environ. Sci. Technol. 52 (2018) 1479–1487.

[51] F. Zhang, F. Xie, S. Zhu, J. Liu, J. Zhang, S. Mei, W. Zhao, A novel photofunctional $g\text{-}C_3N_4/Ag_3PO_4$ bulk heterojunction for decolorization of Rh.B, Chem. Eng. J. 228 (2013) 435–441.

[52] Y. Gao, G. Yu, K. Liu, S. Deng, B. Wang, J. Huang, Y. Wang, Integrated adsorption and visible-light photodegradation of aqueous clofibric acid and carbamazepine by a Fe-based metal-organic framework, Chem. Eng. J. 330 (2017) 157–165.

[53] M. Nawaz, W. Miran, J. Jang, D.S. Lee, One-step hydrothermal synthesis of porous 3D reduced graphene oxide/TiO_2 aerogel for carbamazepine photodegradation in aqueous solution, Appl. Catal. B: Environ. 203 (2017) 85–95.

[54] D. Du, W. Shi, L. Wang, J. Zhang, Yolk-shell structured Fe_3O_4@void@TiO_2 as a photo-Fenton-like catalyst for the extremely efficient elimination of tetracycline, Appl. Catal. B: Environ. 200 (2017) 484–492.

[55] Y. Zhu, R. Zhu, Y. Xi, T. Xu, L. Yan, J. Zhu, G. Zhu, H. He, Heterogeneous photo-Fenton degradation of bisphenol A over Ag/AgCl/ferrihydrite catalysts under visible light, Chem. Eng. J. 346 (2018) 567–577.

[56] Y. Zhu, R. Zhu, L. Yan, H. Fu, Y. Xi, H. Zhou, G. Zhu, J. Zhu, H. He, Visible-light Ag/AgBr/ferrihydrite catalyst with enhanced heterogeneous photo-Fenton reactivity via electron transfer from Ag/AgBr to ferrihydrite, Appl. Catal. B: Environ. 239 (2018) 280–289.

[57] K. Zhang, Y. Liu, J. Deng, S. Xie, H. Lin, X. Zhao, J. Yang, Z. Han, H. Dai, Fe_2O_3/3DOM $BiVO_4$: High-performance photocatalysts for the visible light-driven degradation of 4-nitrophenol, Appl. Catal. B: Environ. 202 (2017) 569–579.

[58] Y. Lin, S. Wu, C. Yang, M. Chen, X. Li, Preparation of size-controlled silver phosphate catalysts and their enhanced photocatalysis performance via synergetic effect with MWCNTs and PANI, Appl. Catal. B: Environ. 245 (2019) 71–86.

[59] X. Wang, T.-T. Lim, Solvothermal synthesis of C–N codoped TiO_2 and photocatalytic evaluation for bisphenol A degradation using a visible-light irradiated LED photoreactor, Appl. Catal. B: Environ. 100 (2010) 355–364.

[60] A. Rincon, Effect of pH, inorganic ions, organic matter and H_2O_2 on E. Coli K12 photocatalytic inactivation by TiO_2 Implications in solar water disinfection, Appl. Catal. B: Environ. 51 (2004) 283–302.

[61] Y. Yang, J.J. Pignatello, J. Ma, W.A. Mitch, Comparison of halide impacts on the efficiency of contaminant degradation by sulfate and hydroxyl radical-based advanced oxidation processes (AOPs), Environ. Sci. Technol. 48 (2014) 2344–2351.
[62] P. Neta, V. Madhavan, H. Zemel, R.W. Fessenden, Rate constants and mechanism of reaction of $\cdot SO_4^-$ with aromatic compounds, J. Am. Chem. Soc. 99 (1977) 163–164.
[63] C. Jiang, Y. Ji, Y. Shi, J. Chen, T. Cai, Sulfate radical-based oxidation of fluoroquinolone antibiotics: kinetics, mechanisms and effects of natural water matrices, Water Res. 106 (2016) 507–517.
[64] H. Wang, Y. Wu, M. Feng, W. Tu, T. Xiao, T. Xiong, H. Ang, X. Yuan, J.W. Chew, Visible-light-driven removal of tetracycline antibiotics and reclamation of hydrogen energy from natural water matrices and wastewater by polymeric carbon nitride foam, Water Res. 144 (2018) 215–225.
[65] Y. Li, B. Zhang, X. Liu, Q. Zhao, H. Zhang, Y. Zhang, P. Ning, S. Tian, Ferrocene-catalyzed heterogeneous Fenton-like degradation mechanisms and pathways of antibiotics under simulated sunlight: a case study of sulfamethoxazole, J. Hazard. Mater. 353 (2018) 26–34.
[66] S. Canonica, T. Kohn, M. Mac, F.J. Real, J. Wirz, U.V. Gunten, Photosensitizer method to determine rate constants for the reaction of carbonate radical with organic compounds, Environ. Sci. Technol. 39 (2005) 9182–9188.
[67] Y. AlSalka, L.I. Granone, W. Ramadan, A. Hakki, R. Dillert, D.W. Bahnemann, Iron-based photocatalytic and photoelectrocatalytic nano-structures: Facts, perspectives, and expectations, Appl. Catal. B: Environ. 244 (2019) 1065–1095.